

Diode Laser-Waveguide Spectroscopy in Solid Argon Slabs

John Khademi, Mark Fisher, Bill Kapelle, and V. A. Apkarian*

Department of Chemistry, University of California, Irvine, California 92717 (Received: June 26, 1987)

It is possible to deposit high-quality argon films on metal surfaces to be used as thin dielectric slab waveguides. The combination of diode lasers with argon waveguides represents a convenient spectroscopic technique of high sensitivity and resolution, ideally suited for vibrational spectroscopy of adsorbates. In a first-generation waveguide assembly we demonstrate the single-mode guiding properties of argon slabs deposited on copper mirrors. The utility of the technique is demonstrated by recording absorption spectra of CH_3F molecules doped in the guide. A comparison between spectra obtained by reflection versus transverse magnetic guided waves is made to illustrate the salient features of this technique.

I. Introduction

Rare gas films deposited on metal mirrors constitute classical dielectric slab waveguides. This was recognized by Rossetti and Brus, who demonstrated that, by taking advantage of waveguiding in thick rare gas slabs, enhanced sensitivities in optical absorption and scattering spectroscopies of matrix-isolated species could be derived.¹ Bondybey and co-workers subsequently applied this technique in UV-vis absorption spectroscopy of matrix-isolated ionic species.^{2,3} In this paper we consider the characteristics of thin argon slabs as infrared waveguides both theoretically and experimentally. Slab waveguides may be classified as thick or thin according to whether $\lambda/d \gg 1$ or $\lambda/d \sim 1$, where d is the thickness of the slab and λ is the wavelength of the radiation propagating in the slab. Only thick rare gas slabs, $\lambda/d \gtrsim 10^2$, were considered in the past.¹⁻³ There are significant differences between the characteristics of waveguides in these two different limits. Thick guides sustain multimode propagation, are not wavelength selective, and therefore are useful for spectroscopic investigations in broad spectral ranges; however, their sensitivity advantages are inherently limited to bulk studies and practically limited to wavelengths shorter than $1 \mu\text{m}$. Thin guides are both wavelength and mode selective and therefore limited to spectroscopic studies in narrow spectral ranges; however, their sensitivity advantages apply to both bulk and surface studies and can be conveniently applied from the far-IR to the UV spectral ranges.

We demonstrate that the combination of tunable diode lasers and thin rare gas waveguides represents a powerful spectroscopic technique of high resolution and high sensitivity. The resolution is limited by the line width of the laser (10^{-4} cm^{-1} in the present studies). The sensitivity of the technique is calibrated by studies in which the argon slab is doped with CH_3F . It is shown that a total of 10^{13} molecules in the radiation field is sufficient to yield a high signal-to-noise ratio in this first generation experimental design. The technique therefore has the requisite sensitivity for the detection of submonolayer coverages of adsorbates sandwiched between the metal/matrix interface. Whether chemisorbed or physisorbed, it is safe to expect only minor perturbation on the vibrational spectra of the sandwiched species from the rare gas waveguide overlayer. The extent of this perturbation can be gauged from the extensive tabulations of matrix vibrational shifts by M. Jacox.⁴

The advantages and enhanced sensitivity of waveguide spectroscopy can be understood via a comparison with conventional matrix isolation spectroscopy and grazing incidence IR surface spectroscopy. Matrix isolation is a well-established sensitive technique for vibrational spectroscopy of molecular species.^{4,6} The sensitivity is derived from two factors: high packing densities of

rare gas solids and the absence of rotational partitioning of internal populations of the trapped molecular species.

Traditionally two geometries are used, transmission (Figure 1A) and reflection (Figure 1B). In the case of transmission, the matrix is deposited on a transparent substrate such as CsI and the absorption path length, l , is given by the thickness of the solid, d . In the case of reflection, the sample is deposited on a polished metallic mirror, and hence for a given sample thickness, d , the absorption path length, l , is more than doubled: $l = 2nd/\cos \phi$, in which ϕ is the diffraction angle. Obviously, the thicker the sample, the larger the absorption. However, there are practical limits imposed on sample thickness. The most serious of these is the poor thermal conductivity of rare gas solids such that beyond a thickness of $10^2 \mu\text{m}$ scattering losses begin to dominate. For purposes of UV-vis spectroscopy, such a thickness is sufficient to record spectra along the length of the matrix which acts as a thick slab waveguide.¹⁻³

In thin waveguides, the probe beam is contained in the rare gas film by coupling into the resonant modes of a cavity created by the matrix/vacuum and metal/matrix interfaces. Since the required thickness of the solid is of the order of the wavelength of the radiation utilized, very flat and transparent films can be deposited. In this geometry, the probe beam travels nearly parallel to the substrate surface and the absorption path length, l , is determined by the injection angle: $D \leq l \leq D/\sin \theta$, in which θ is the critical angle at the matrix/vacuum interface (see Figure 1D). The drawback of the wavelength dependence of the containment of the radiation in thin slabs can be overcome by increasing the thickness of the slab to adopt the attenuated total internal reflection geometry (ATIR). The path length in this case is given as $l = D/\sin \theta$ (see Figure 1C) and again is independent of thickness as long as $d \gg \lambda$. The ATIR geometry can be regarded as a limiting case of waveguiding and can be discussed in the same formalism. The efficient execution of either waveguide or total internal reflection spectroscopy would require injection couplers that guarantee injection angles greater than the critical angle of the rare gas layer. However, as will be shown, even in the absence of such couplers the technique can be used.

In the case of surface spectroscopy, in recent years, the grazing incidence reflection technique has been developed successfully and has provided some of the highest resolution surface vibrational spectra.⁷⁻⁹ The success of the technique is based on the long interaction length between the incident radiation and surface adsorbates. Clearly, waveguiding provides a significant improvement over these techniques. ATIR has also been discussed as a surface sensitive technique, however, with the limitation that only adsorbates on transparent substrates can be studied.¹⁰ Waveguiding in a rare gas overlayer overcomes these limitations, is simple to execute, and in addition to the higher detection

(1) Rossetti, R.; Brus, L. E. *Rev. Sci. Instrum.* **1980**, *51*, 467.

(2) Bondybey, V. E.; Miller, T. A. In *Molecular Ions: Spectroscopy, Structure and Chemistry*; Miller, T. A., Bondybey, V. E., Eds.; North-Holland: New York, 1983; p 129.

(3) Bondybey, V. E.; Miller, T. A.; English, J. M. *J. Chem. Phys.* **1980**, *72*, 2193.

(4) Jacox, M. E. *J. Mol. Spectrosc.* **1985**, *113*, 286.

(5) Meyer, B. *Low Temperature Spectroscopy*; Elsevier: New York, 1971.

(6) *Vibrational Spectroscopy of Trapped Species*; Hallam, H. E., Ed.; Wiley-Interscience: New York, 1973; p 171.

(7) Greenler, R. G. *J. Chem. Phys.* **1966**, *44*, 310.

(8) *Vibrations at Surfaces*; Caudano, R., Gilles, J. M., Lucas, A. A., Eds.; Plenum: New York, 1982.

(9) Hoffmann, F. M.; Levinos, N. J.; Perry, B. N.; Rabinowitz, P. *Phys. Rev. B: Condens. Matter* **1986**, *33*, 4309.

(10) Harrick, N. J. *Ann. N.Y. Acad. Sci.* **1963**, *101*, 928; *J. Opt. Soc. Am.* **1965**, *55*, 851.

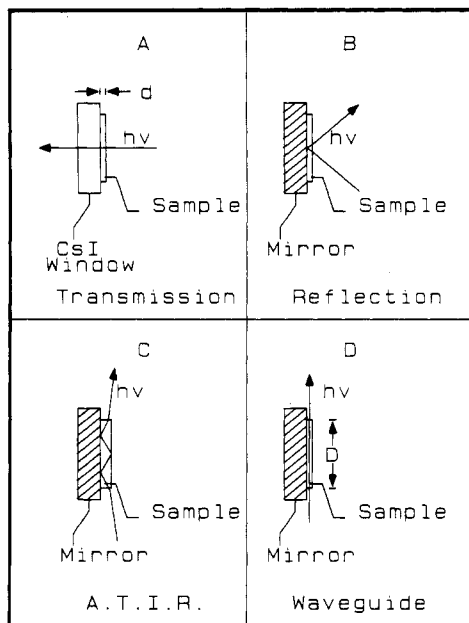


Figure 1. Different schemes of spectroscopy for a matrix of thickness d and length D .

sensitivity can be used in applications where high field densities are required, as in nonlinear spectroscopies.¹¹ It is important to note that in order for the technique to be useful for surface spectroscopy, the electric field of the propagating radiation at the waveguide/metal interface should be nonvanishing. This is the case for transverse magnetic (TM) guided modes which can be selected by controlling the polarization of the injection radiation.

The organization of this report is as follows. Under the heading of Theory, expressions governing waveguiding in the present slab geometry are developed. In the Experimental Section we describe the design of a simple waveguiding assembly and the methods used for obtaining high-quality slabs. The observed guiding resonances in pure and doped waveguides are presented in the Results section and discussed in relation to waveguiding expressions presented in the Theory section. Finally, the applications and improvements of the present technique are discussed in the Conclusions section.

II. Theory

The principles of dielectric waveguides are well-understood and can be found in standard texts of electrodynamics.¹²⁻¹⁴ The solutions of the guided modes are obtained by solving the Maxwell equations subject to the boundary conditions dictated by the geometry of the dielectric medium. The case of a planar waveguide, a slab, is particularly simple since the equations are separable into two independent sets of solutions: transverse electric, TE_m , and transverse magnetic, TM_m , where m is the mode number. The present geometry, namely that of a dielectric slab with a mirror at one interface and vacuum at the other, can be treated by minor adaptation to the well-known solutions of the symmetric slab.

The guiding conditions for a dielectric slab of index n , with a perfectly conducting mirror at one interface and vacuum, medium of index 1, on the other, are derived by imposing the conditions that (a) the electric field parallel to the conductor surface at the mirror/slab interface be zero, (b) the field components inside the slab be sinusoidal, and (c) the field components decay exponentially into the vacuum. The resulting field components for TE and TM modes are derived by imposing the boundary conditions

on the y field component and demanding tangential continuity at the slab/vacuum interface.

TE modes (E_y, H_z, H_x):

$$E_y = 0 \quad x = 0 \quad (1)$$

$$E_y = A \sin(hx)e^{i(\omega t - \beta z)} \quad 0 \leq x \leq d \quad (2)$$

$$E_y = A \sin(hd)e^{-p(x-d)}e^{i(\omega t - \beta z)} \quad d \leq x \quad (3)$$

in which h , p , and β are real positive propagation constants: h along the x axis in the slab, p along the x axis in the vacuum, and β along the z axis. The condition for continuity of H_z at the vacuum interface is satisfied by matching $H_z = (2/\omega\mu)(\delta E_y/\delta x)$ in the two media and yields

$$h \cos(hd) = -p \sin(hd) \quad (4)$$

or equivalently

$$-hd \cot(hd) = pd \quad (5)$$

Furthermore, the propagation constants need satisfy the reduced wave equation in each medium

$$\frac{\delta^2 E_y}{dx^2} + \frac{\delta^2 E_y}{dz^2} + n_i^2 k_0^2 E_y = 0 \quad (6)$$

in which the subscript i refers to dielectric or vacuum and k_0 is the propagation constant in vacuum, $k_0 = 2\pi/\lambda$. Equation 6 then provides the additional constraints

$$\beta^2 = n^2 k_0^2 - h^2 \quad (7)$$

$$\beta^2 = k_0^2 + p^2 \quad (8)$$

which can be combined to yield

$$h^2 d^2 + p^2 d^2 = (n^2 - 1)k_0^2 d^2 \equiv u^2 \quad (9)$$

The transcendental eigenvalue equation, eq 5, and the constraint of eq 9 together yield the desired guided mode solutions. The most common method of representing these solutions is graphically: the solutions correspond to intersections of the negative cotangent function with circles of radius u in a pd versus hd plane.¹³ Note that the present solutions correspond to only the odd modes of the symmetric slab.

TM modes (E_z, E_x, H_y):

$$H_y = B e^{i(\omega t - \beta z)} \quad x = 0 \quad (10)$$

$$H_y = B \cos(hx)e^{i(\omega t - \beta z)} \quad 0 \leq x \leq d \quad (11)$$

$$H_y = B \cos(hd)e^{-p(x-d)}e^{i(\omega t - \beta z)} \quad d \leq x \quad (12)$$

We note that these equations satisfy the desired conditions for the longitudinal electric field component, E_z , namely

$$E_z = 0 \quad x = 0 \quad (13)$$

$$E_z = \frac{ih}{n^2 \omega \epsilon_0} B \sin(hx)e^{i(\omega t - \beta z)} \quad 0 \leq x \leq d \quad (14)$$

$$E_z = \frac{ip}{\omega \epsilon_0} B \cos(hd)e^{-p(x-d)}e^{i(\omega t - \beta z)} \quad d \leq x \quad (15)$$

and the continuity of E_z at the vacuum interface yields

$$h \tan(hd) = n^2 p \quad (16)$$

The wave equation constraints, eq 7-9, are appropriate for TM modes also. The acceptable solutions in this case correspond to the even modes of the symmetric slab.

Note that while in the case of TE modes the only electric field component, E_y , is zero at the mirror/slab interface in the case of TM modes, the E_x field component is nonvanishing:

$$E_x = \frac{i}{n^2 \omega \epsilon_0} \frac{\delta H_y}{\delta z} = \frac{\beta B e^{i(\omega t - \beta z)}}{n^2 \omega \epsilon_0} \quad x = 0 \quad (17)$$

Thus, for the purposes of spectroscopy of molecular adsorbates

(11) See for example: Normandin, R.; Stegeman, G. I. *Appl. Phys. Lett.* **1980**, *36*, 253. Hetherington, W. W.; Ho, Z. Z.; Koenig, E. W.; Stegeman, G. I.; Fortenberry, R. M. *Chem. Phys. Lett.* **1986**, *128*, 150.

(12) Marcuse, D. *Light Transmission Optics*; Van Nostrand Reinhold: New York, 1972.

(13) Yariv, A. *Optical Electronics*, 3rd ed.; Holt, Rinehart and Winston: New York, 1985; Chapter 13.

(14) Lotspeich, J. F. *Appl. Opt.* **1975**, *14*, 327.

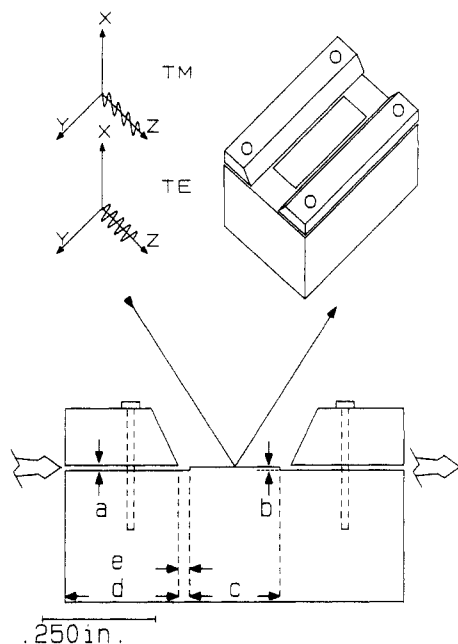


Figure 2. Waveguide assembly. A perspective view of the assembly is shown at the top, along with the coordinate system used in the discussion. x -polarized light is used to launch TM modes while y -polarized light is used for TE modes. A cross-sectional view of the block (x - z plane) is provided in the lower half. The drawing is to scale; the scale is shown. Dimension a is adjustable and typically ranges between 0.011 and 0.025 in. The other dimensions are fixed: $b = 0.0077$ in., $c = 0.200$ in., $d = 0.250$ in., $e = 0.025$ in. Also shown are the directions of the He:Ne beam (single line arrow) and the IR beam (broken arrows).

on the metal surface, TE modes are not useful while TM modes are. Moreover, it is to be expected that the effective field experienced by the molecular adsorbates at this interface will be further enhanced due to the image field created in the metal which reinforces E_x . It is therefore important to demonstrate the spectroscopic capability of these waveguides in the case of TM coupling. The guiding properties of pure Ar waveguides with respect to both TE and TM modes will be presented. In the case of CH_3F -doped Ar waveguides only TM modes are utilized in recording the absorption spectra.

III. Experimental Section

In the present experiments, either pure Ar or CH_3F -doped Ar films are used as the waveguiding layer, and a polished block of OFHC copper is used as substrate. The waveguide assembly is shown in Figure 2. The edges of a $3/4 \times 1$ -in. copper block were recessed by 0.0077 in. to leave a 0.200×0.500 -in. platform. Two polished copper rails are attached to the recessed edges with 0–80 brass screws and spaced with brass washers to create an adjustable clear gap between the bottom of the rails and the top of the platform. Typical gaps (difference between dimensions a and b indicated in Figure 2, top) ranged between 200 and 80 μm . The rails serve the dual purpose of providing slits for coupling the radiation in and out and masking the block during deposition to provide waveguide edges. The entire assembly is mounted on the cryotip of either a closed cycle (Air Products Displex DE202) or a liquid He (Air Products Helitran) cryostat. An indium gasket is crushed between substrate and cryotip to ensure good thermal contact. The vacuum shroud of the cryostat is fitted with four IR transmitting windows which are sealed by O-rings. The system vacuum is maintained below 10^{-6} Torr throughout the experiments.

The rare gas solids are formed by pulsed deposition of the room-temperature gas on the cooled substrate through two solenoid valves. The dead volume between the deposition valves is 1.26 cm^3 . The backing pressure is monitored via a capacitance manometer and maintained between preset levels through a third solenoid valve. The latter is directly attached to the neck of a 2-L reservoir. The deposition rate and backing pressures are computer-controlled. Typical deposition conditions that yielded

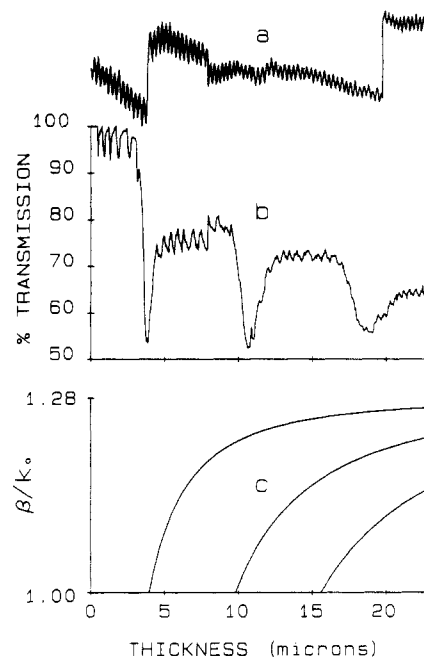


Figure 3. Transmission of TE modes. Trace a shows the intensity of the reflected He:Ne beam. These fringes are used to define the abscissa of the plots. Trace b corresponds to the intensity of the transmitted IR beam; a transmission of 100% corresponds to the intensity prior to deposition of the argon layer. Trace c is a plot of β , the theoretical propagation constant, for the first three odd modes.

reproducibly flat and nonscattering films were as follows: backing pressure between 7 and 12 Torr (pulse sizes between 0.0088 and 0.0151 Torr-L), pulse rate 0.08 Hz, and deposition temperatures that ranged between 12 and 19 K. As a precautionary measure to avoid the condensation of background impurities, Ar gas is pulsed at the substrate during cool down.

The thickness of the rare gas solid is measured by monitoring interference fringes from a reflected He:Ne laser. The thickness, d , is obtained from the number of observed fringes according to $d = n\lambda/2 \cos \phi$ (n is the index of refraction, $\lambda = 0.6328 \mu\text{m}$, ϕ is the refraction angle). ϕ was obtained from the angle of incidence, θ , and the latter was obtained geometrically by measuring the separation between incoming and outgoing beams. Since $\theta \approx 45^\circ$ in all experiments, for a given value of n , the reported thickness errors are estimated to be within 5%. In addition to the determination of thickness, the He:Ne fringe modulation depth is an indication of the flatness of the interfaces within the beam diameter of 1 mm. As can be seen in Figures 3a and 4a, the modulation depth is maintained for the duration of deposition, 97 and 121 fringes in Figures 5a and 6a, respectively.

A tunable diode laser operating at $9.6 \mu\text{m}$ is used as the IR source (Spectra Analytics). The laser is partially polarized, $>10:1$, and its polarization rotated by two 45° mirrors. The IR beam is focused on the input slit of the waveguide assembly by a single-element Ar-coated ZnSe lens ($f.l. = 2.5$ in., $\phi = 2$ in.), mounted on a precision x,y,z stage with tilt adjustments. The throughput of the waveguide assembly is focused on a Hg:Cd:Te detector and maximized prior to deposition. The beam waist at the waveguide is near its diffraction limit. The size of the focal waist is estimated by measuring the diode laser profile at four different distances past the lens (two prior to the focal plane and two post focus) with a 0.1-mm pinhole. A typical beam waist at the input slit is 40 μm and expands to 50 μm at the output slit. Both IR and He:Ne beams are mechanically chopped, amplified with a lock-in amplifier, digitized, stored, and displayed simultaneously by the computer.

It should be obvious from the design of the guiding assembly that only radiation that propagates the full length of the slab, 5 mm, is detected through the output coupler. The injection angle at the waveguide is ill-defined since the edges of the deposited waveguide are not restricted. It is, however, possible to analyze

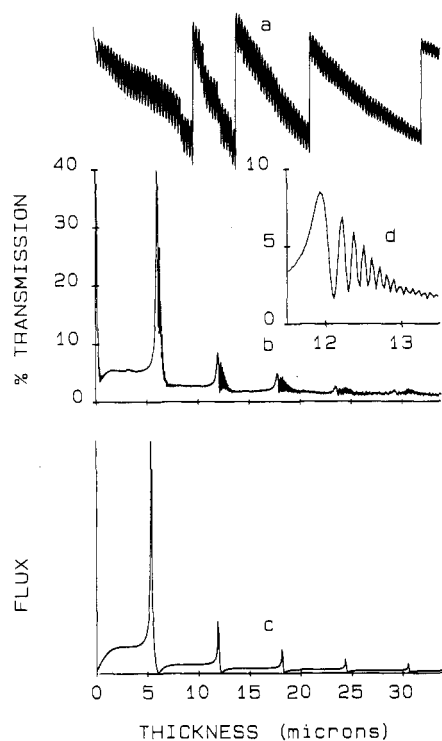


Figure 4. Transmission of TM modes: (a) Intensity of the reflected He:Ne beam. The discontinuities are due to repositioning of the beam on the photodiode made necessary by beam walk. (b) Intensity of the transmitted IR beam. A transmission of 100% corresponds to the intensity prior to deposition of the Ar film. (c) The theoretical flux of the slab for even TM modes, eq 22, allowing for both confined and radiation modes. The ordinate scale is arbitrary, however, normalized to match the height of TM_0 . (d) Expansion of the 10–13- μm range of the experimental trace in (b).

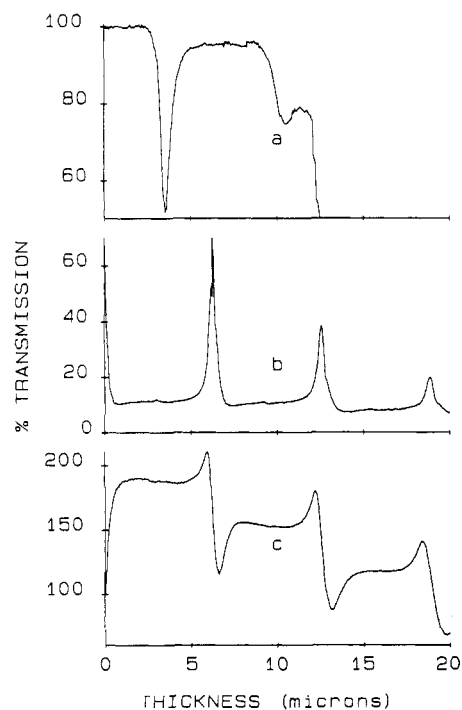


Figure 5. Experimental transmission of the waveguide for different injections. (a) TE modes are shown in a slab that cracked immediately after the cutoff of TE_3 . (b) TM modes. (c) TM injection on an oxidized copper surface. The slit width, dimension a of Figure 4, was adjusted to 0.025 in. in all three experiments.

the transmission of the assembly by considering the total contained power of the injected beam. The transmission of the assembly is defined as $I(d)/I_0$, in which I_0 is the throughput of the assembly prior to deposition of the film and $I(d)$ is the total transmitted

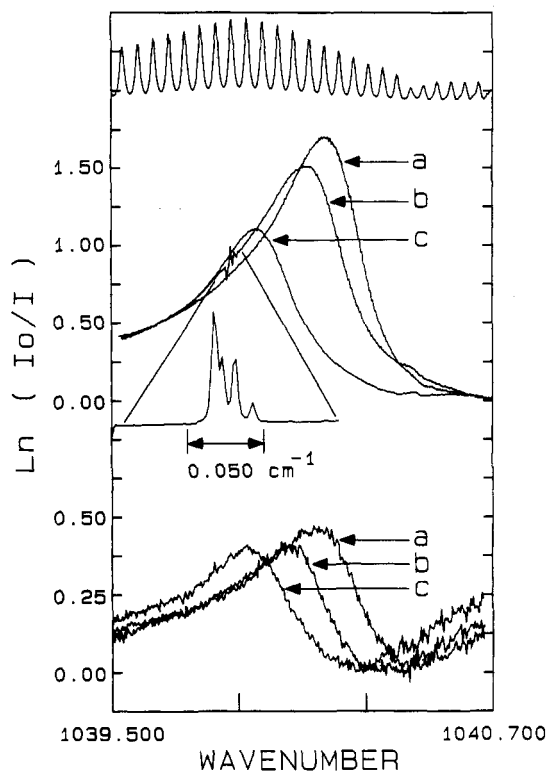


Figure 6. Absorption spectra in 1:1000 $\text{CH}_3\text{F}:\text{Ar}$ film. The top trace corresponds to fringes obtained from a Ge etalon, $\text{FSR} = 0.048 \text{ cm}^{-1}$. The absorption spectra were recorded at three different temperatures: (a) 13 K, (b) 17 K, (c) 25 K. The upper a, b, c traces are the spectra recorded in the reflection geometry (path length 65 μm). The lower a, b, c spectra were recorded in the waveguiding geometry ($d = 13 \mu\text{m}$). Absolute calibration of the spectra is achieved by reference to the gas-phase P(5) transition of CH_3F which is shown on an expanded wavelength scale in the middle portion of the figure.

intensity at a given thickness of the slab, d . Radiation propagating through the slab and above the slab are both collected. The collection angle is restricted by the output slits to be less than 2.3° for a slit width of 0.011 in. (dimension a of Figure 2).

IV. Results and Discussion

A. Waveguiding. The experimental transmission of the assembly for y -polarized injected radiation, and therefore TE guided modes, is shown in Figure 3b. The thickness of the slab is derived from the He:Ne fringes shown in Figure 3a. The transmission features of this geometry can be understood by comparison to the theoretical propagation constant, β , which is plotted in Figure 3c. The far from cutoff approximation¹²

$$hd = \frac{\pi}{2}(m+1) \frac{u}{1+u} \quad m = 1, 3, 5, \dots \quad (18)$$

is used for the evaluation of β through eq 7. While approximate, this evaluation serves the purposes of interpreting the experimental data. The values of β are bracketed such that $k_0 < \beta < nk_0$, and therefore only guided modes are considered.

It can be seen that for the first 3- μm thickness of the slab the transmission remains constant. The only effect of the deposited film is fringes which can be interpreted as due to interference between radiation directly transmitted above the film and radiation reflected from the substrate. The present geometry closely resembles Lloyd's mirror experiment,¹⁵ and the fringes can be explained as such. Near a thickness of 3 μm , which corresponds to be cutoff of the first odd mode, TE_1 , the transmission declines to $\sim 50\%$ and follows the confinement curve of β . Subsequent dips occur past the cutoffs of the second and third odd guided

(15) A discussion of Lloyd's experiment can be found in standard texts on optics. See for example: Jenkins, F. A.; White, H. E. *Fundamentals of Optics*; McGraw-Hill: New York, 1976.

modes, TE₃ and TE₅, and each time the transmission recovers to a level ~10% lower than the prior, following the trend of reduced confinement for higher modes seen in the theoretical plot. As expected, the even TE modes are absent due to the required reflection symmetry (see section II). The fact that the transmission follows the propagation of higher modes as they become confined implies that the slab acts as a single-mode guide even for thicknesses where several modes can be sustained simultaneously. This is not expected for a slab with perfectly flat interfaces. It is well-known that surface imperfections induce mode coupling and the conversion of power from lower modes to higher ones even though the latter are less confined.^{12,13} An obvious source of imperfection in the present case is due to the deposition geometry. The deposition nozzle can be regarded as a point source directed at the copper substrate, and therefore the spray should produce a slab thicker in the center than at the edges. Such a curvature is sufficient to serve as coupling among guided modes and also between a given guided mode and the continuum of radiation modes. The dips can then be interpreted as power loss to radiation modes during the transition from a given guided mode to another. The coupled mode solutions are complicated even for model imperfections such as sinusoidal corrugation of interfaces.¹² Instead of a rigorous treatment of the problem, we give a more physical picture of the guiding process which at least qualitatively explains the main features of the experimental throughput.

The wave propagation inside the dielectric slab can be regarded as due to a plane wave with propagation constant nk_0 traveling at an angle θ from the z axis and undergoing multiple internal reflections. This interpretation is explicit in the relation between the three propagation constants in the slab, eq 7, which corresponds to a right angle triangle of hypotenuse nk_0 and sides β and h . In terms of the angle between nk_0 and β , this relationship can be expressed as $\beta = nk_0 \cos \theta$. Travel at the critical angle corresponds to $\theta = \arccos(1/n)$ or, equivalently, to $\beta = k_0$. This condition defines the cutoff of a given guided mode. Confinement is only possible for $\beta > k_0$ while for $\beta < k_0$ the power is coupled to radiation modes as opposed to guided modes. The cutoff condition then implies, according to eq 8, that $p = 0$ and according to eq 9 that $hd = u$. The near-cutoff condition then can be expressed by substitution of eq 5 in eq 8

$$\beta = (k_0^2 + h^2 \cot^2 u)^{1/2} \quad (19)$$

from which the cutoff of the different modes ($\beta = k_0$) can be derived as

$$u = (n^2 - 1)^{1/2} hd = \frac{m\pi}{2} \quad m = 1, 3, 5, \dots \quad (20)$$

For $\lambda = 9.6 \mu\text{m}$ and $n = 1.28$, it can then be calculated from eq 20 that the cutoff of the first odd mode, TE₁, occurs at $3 \mu\text{m}$ with subsequent cutoffs spaced $6 \mu\text{m}$ apart. The minima in transmission of Figure 3b which occur just past the cutoff of the different odd modes implies an abrupt change in β and the launching of higher modes. In the process, power is lost to radiation modes which propagate outside the slab. Propagation of guided modes far from cutoff, $\beta \approx nk_0$, implies travel of the plane wave parallel to the interfaces. While confinement is greatest in this case for a perfect waveguide, the guiding is sensitive to the overall flatness of the interfaces. The required length of flatness is then directly proportional to nk_0/β , hence the instability of a given mode far from cutoff in the presence of an imperfection and the coupling of power to higher modes for which β is necessarily smaller.

The experimental transmission of the waveguide for injection of x -polarized, and therefore TM, modes is shown in Figure 6b. The associated He:Ne fringes are shown in Figure 4a. The transmission in this case is characteristically different from that of TE modes. The transmitted flux sharply declines as the thickness of the slab is increased. Immediately after the first drop the throughput increases to ~5% following the confinement of TM₀. Maxima can be seen spaced at $6 \mu\text{m}$, at the cutoffs of even TM modes. Closer inspection reveals a smaller modulation centered between the maxima at the cutoffs of odd TM modes. In the case of TM modes, the confined field is always coupled

to the metal through the image field of E_x . Thus, while efficient confinement is possible, a poor transmission is to be expected since the field decays into the metal—evanescent modes do not carry any power. The observed maxima then correspond to radiation modes which are launched when the confined radiation switches to higher modes. The radiation modes are further identified by the fringes that follow (see the inset in Figure 4), which can again be ascribed to Lloyd's fringes. The heights of the maxima are then a measure of the extent of confinement of a given mode. The observed throughput of the waveguide can be reproduced by considering the power flux along z . For a given injected power P

$$P = \frac{1}{2} \int_0^\infty (E \times H^*)_z dx = \int_0^\infty E_x H_y^* dx \quad (21)$$

the flux can be calculated as $\langle S \rangle = B^2 |\beta|$ in which B is the amplitude of the H_y field component (see eq 10–12)

$$\langle S \rangle = \frac{n^2 p}{pd + \frac{n^2(n^2 - 1)k_0}{(n^2 - 1)k_0 + (n^4 - 1)p^2}} = 2\omega\epsilon_0 P \quad (22)$$

with the eigenvalue relation of eq 16 and the assumption of near-cutoff condition, eq 22 can be evaluated with the substitution

$$n^2 p = \frac{u \tan u}{d} \quad (23)$$

Both guided and radiation modes can be included in the evaluation by allowing both positive and negative values of p in eq 23. Note a negative value of p implies that the field grows exponentially in the vacuum. The function of eq 22 is not bounded and tends to infinity as $u \rightarrow \pi$. However, the difficulty can be simply overcome by evaluating $\langle S \rangle$ within $\pm\delta$ of the singularities. The theoretical plot of the flux is shown in Figure 4c. P was used as a normalization constant and δ ($\delta = 10^{-5} \mu\text{m}$) was chosen to match the first peak height and maintained a constant throughout. It can be seen that, with the exception of the Lloyd's fringes (shown in Figure 4d), the experimental throughput is well-reproduced by eq 22. It is then possible to confirm that the maxima correspond to radiation modes where $\beta < k_0$. The subsequent peak heights drop as $1/d$ (the limit of eq 22 for $\tan(u) \rightarrow \pm\infty$) and represents the extent of confinement of the guided modes. The switchover from guided to radiation modes occurs at 3, 9, ... μm , where small modulations are observed in the experimental transmitted intensity.

The overall features of the transmission observed for TE and TM modes are insensitive to exact dimensions of the assembly; however, as expected, both transmission and confinement depend on the quality (crystallinity) of the slab. In Figure 5, the transmission of the assembly for wider slit width (dimension a of Figure 2 = 0.025 in.) is shown. TE modes are shown in Figure 5a. These are very similar to those shown in Figure 3b; however, the fringes are absent and the transmission of TE₁ is greater than 90%. The drop in intensity immediately following the cutoff of TE₃ is due to cracking of the slab. Once cracked, the transparency of the slab cannot be recovered by annealing. In Figure 5b the transmission of TM modes is shown. Due to the larger slits, the fringes observed in Figure 4b are absent. The transmission of TM₀ is ~10%, and the confinement, as obtained from the height of the first radiation mode, is ~70%.

Eventual oxidation of the copper assembly in our 10^{-6} -Torr vacuum system is unavoidable. All of the data presented above refer to studies performed over freshly polished substrates. Figure 5c illustrates the transmission characteristics of TM modes in a slab deposited over a substrate that was allowed to oxidize under vacuum over the course of several days. The transmission in this case more than doubles for TM₀ in contrast with the case of a clean copper surface. It can then be inferred that the oxide layer is thick enough to prevent dissipation of the contained field by coupling to the image field. The fact that the radiation field couples into the argon overlayer implies that the oxide thickness is less than the confinement limit of TM₀; $d_0 < \lambda/4(n_0^2 - n_A^2)^{1/2} \sim 1 \mu\text{m}$ (the subscripts 0 and A refer to oxide and Ar, respectively,

$n_0 = 2.8$).¹⁶ An exact analysis of the features would require the treatment of an asymmetric waveguide which is beyond the scope of this report. However, the general features can be understood by assuming that upon initial alignment of the assembly the radiation is guided in the oxide layer, which is subsequently coupled into the argon layer due to the reduction of the effective index of the oxide guide. An almost exact tangent function is observed, as expected for even TM modes and the flux decays as $1/d$ as in the case of the mirror.

B. Spectroscopy. CH_3F -doped argon slabs were used to test the utility of the TM modes in spectroscopic applications. The choice of this system was based on the fact that extensive literature exists on the IR spectroscopy of matrix-isolated CH_3F .¹⁷ The ν_3 mode, the C-F stretch, has previously been studied by FTIR.¹⁷ It was believed that in annealed matrices the line width of this transition could be narrowed to less than 0.1 cm^{-1} . Narrow line widths are particularly well-suited for diode laser spectroscopy due to the limited range of single-mode tuning in such lasers. The fringes obtained from a germanium etalon ($\text{FSR} = 0.048 \text{ cm}^{-1}$), in the spectral range that corresponds to the $\text{CH}_3\text{F}(\nu_3)$ absorption in solid Ar, are shown in the upper trace of Figure 6. From the envelope of the fringes the tuning curve of the diode can be discerned. Mode hopping precludes the continuous scan of a wider range.

Absorption spectra recorded in the reflection geometry in a 1:1000 $\text{CH}_3\text{F}:\text{Ar}$ matrix, recorded at three different temperatures, are shown in Figure 6 (upper a, b, c traces). In order to provide an absolute wavelength calibration, a 20-cm gas cell containing 0.5 Torr of CH_3F was inserted in the laser beam while recording the matrix absorption. The undulations observed in trace b are due to the ratioed gas-phase P(5) absorption which coincides with the $\text{CH}_3\text{F}(\nu_3)$ absorption in solid argon. An expansion of the gas-phase P(5) absorption is also shown in the same figure. The absolute wavelength scale is derived by using the well-known wavelengths of the gas-phase transitions,¹⁸ together with the etalon fringes. The line center and line width of the matrix absorption are temperature-dependent. The dependence is reversible, and even after several annealing cycles at 30 K the line widths remain $\sim 0.5\text{-cm}^{-1}$ fwhm. The characteristic line profile, the long red tail, is also observed in the 1:10 000 solids (*vide infra*). It is believed that in contrast with the FTIR studies the true line shape is being observed for the first time. The analysis of line shapes and their temperature dependence will be taken up in a separate report. However, it is important to note that the line broadening is believed to be homogeneous, based on our failure to burn spectral holes (transient or permanent) in two laser experiments.

The absorption spectrum of the same transition, ν_3 of CH_3F , was also recorded in the waveguide geometry. These spectra at three different temperatures are shown in the lower part of Figure 6. TM modes were used. This was verified by monitoring the transmission of the guide for the first $12\text{-}\mu\text{m}$ thickness of the slab during which time the laser was tuned away from resonance. After establishing that TM modes were being launched by observing the first two spikes of radiation modes, at 6 and $12 \mu\text{m}$, the spectrum was recorded. Therefore, the guided mode corresponds to TM_4 at slab thickness of $\approx 13 \mu\text{m}$. The spectra obtained by the two schemes, reflection of guided TM modes, are similar. However, the signal-to-noise ratio is poorer for the latter, and a closer inspection indicates that the line widths are broader by $\sim 10\%$. The poorer signal-to-noise ratio is due to the fact that only $\sim 1\%$ of the guided TM_4 flux is transmitted in the assembly. The line broadening is due to the very high spectral brightness of the confined power. This was verified by noting that the line width was of the order of the tuning range of the diode ($\sim 1 \text{ cm}^{-1}$) for the TM_0 mode where the confined field density is a factor of 50 larger.

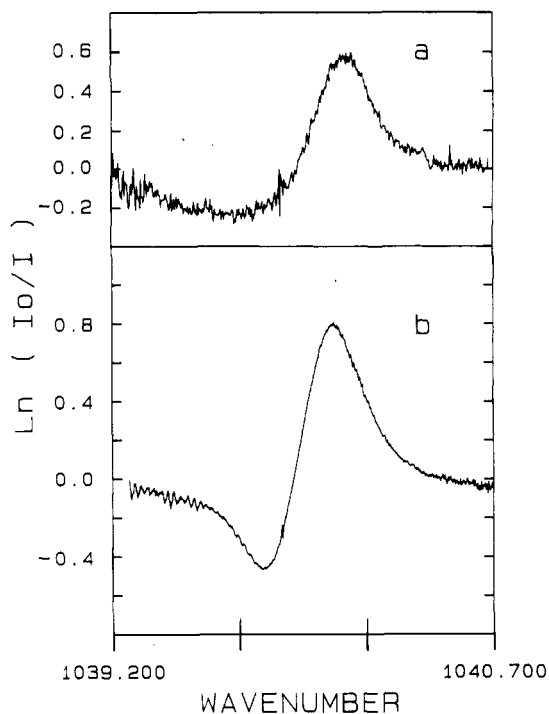


Figure 7. Difference spectra in 1:10 000 $\text{CH}_3\text{F}:\text{Ar}$ slab. The difference in absorption spectra recorded at 13 and 25 K is shown. The top panel is in the waveguiding geometry (TM_4 , $d = 13 \mu\text{m}$). The bottom panel is in the reflection geometry (path length $68 \mu\text{m}$).

Spectra were also recorded in a 1:10 000 $\text{CH}_3\text{F}:\text{Ar}$ slab. The spectra obtained by reflection and guided TM_4 mode were recorded at different temperatures. After ratiating with the background, the spectra recorded at two different temperatures were subtracted from each other. The resultant difference spectra are shown in Figure 7. The comparison of both signal-to-noise ratio and line width is very similar to the case of the 1:1000 solid. It is important to note that very few molecules are being probed in the case of the waveguide geometry. The thickness of the slab is $13 \mu\text{m}$, and the beam waist maintains a width of $5(\pm 1) \times 10^{-3} \text{ cm}$ in the slab. For a packing density of $4 \times 10^{22} \text{ cm}^{-3}$ at 1:10 000 dilution, the total number of molecules in the beam can be estimated as 1×10^{13} molecules. The injected laser power (transmission prior to deposition) corresponds to 2×10^{14} photons/s; hence, the observation of 25% loss due to absorption (see Figure 7) implies that the transition is being saturated. This again is in agreement with the observed line broadening. Given the narrow line width of the laser, typically 10 MHz, saturation of the transition is only possible for a homogeneously broadened line. This conclusion is supported by our failure to observe spectral hole burning.

V. Conclusions

Both TE and TM modes can be guided in thin Ar slabs deposited over metal mirrors. The guiding properties of these slabs are in good agreement with the theoretical expressions developed in section II. While the transmission of the assembly is characteristically different for the two different polarizations, the confinement properties are very similar. More than 70% of the injected power can be confined and therefore guided in the lowest order modes in each case.

TM guided modes are particularly interesting since they imply a nonzero electric field at the metal/dielectric interface and therefore are useful for the IR spectroscopy of metal adsorbates. We have demonstrated that despite the low transmission of TM modes, it is possible to obtain high-resolution IR absorption spectra of molecules doped in the waveguide. Without special signal-averaging techniques, it is possible to record spectra from a total of fewer than 10^{13} molecules in the guided beam. This scheme has the requisite sensitivity for the detection of submonolayer coverages of adsorbates on the metal surface. The resolution of the technique is only limited by the frequency jitter in the diode

(16) *Handbook of Optics*; Driscoll, W. G., Vaughan, W., Eds.; McGraw-Hill: New York, 1978.

(17) Apkarian, V. A.; Weitz, E. *J. Chem. Phys.* **1982**, *76*, 5796. Jones, L. H.; Swanson, B. I. *J. Chem. Phys.* **1982**, *76*, 1634.

(18) Freund, S. M.; Duxbury, G.; Romheld, M.; Tiedje, J. T.; Oka, T. *J. Mol. Spectrosc.* **1974**, *52*, 38.

laser, typically 10^{-4} cm $^{-1}$. The combination of diode lasers with inert rare gas waveguides then represents 4 orders of magnitude improvement in resolution over existing surface sensitive spectroscopic techniques.

It is of interest to also note that in the lowest order guided modes very high field densities are attained in the slab and at the metal/dielectric interface in the case of TM modes. The total injected power in these experiments was typically between 5 and 20 μ W. As much as 70% of this field is contained in the TM $_0$ mode where the thickness of the slab is ~ 3 μ m. For a 50- μ m beam waist, this fluence then corresponds to 6 W/cm 2 . The effect of this high-field density in our present experiments is that of line broadening. These high field densities, coupled with the narrow radiation bandwidth, represent a formidable spectral brightness that could be used in nonlinear spectroscopic applications.¹¹

These demonstrations were performed in a first-generation design of a waveguiding assembly. There are obvious improvements that can be implemented for enhancement of sensitivity and mode selectivity. Prism couplers¹⁹ or a grating etched in the

copper substrate could be used for the injection of radiation at better defined angles and for improved efficiency in output coupling. In order to sample a larger number of molecules either in the slab or at the slab/metal interface, line focusing as opposed to the present point focusing geometry could be used. These improvements, and the incorporation of the assembly in a ultrahigh-vacuum chamber, are presently being implemented in order to apply the technique to submonolayer metal surface adsorbates.

Acknowledgment. Acknowledgment is made to the donors of the Petroleum Research Fund, administered by the American Chemical Society, for partial support of this research. The award from the Camille and Henry Dreyfus Foundation for "Newly Appointed Faculty in Chemistry" is also gratefully acknowledged. The diode lasers were obtained through a grant from the NSF Instrumentation program.

Registry No. Cu, 7440-50-8; Ar, 7440-37-1; CH $_3$ F, 593-53-3.

(19) Tien, P. K.; Ulrich, R.; Martin, R. J. *Appl. Phys. Lett.* 1969, 14, 291.

Reduction Potentials and Exchange Reactions of Thiyl Radicals and Disulfide Anion Radicals

Parminder S. Surdhar and David A. Armstrong*

Department of Chemistry, University of Calgary, Calgary, Alberta, Canada T2N 1N4 (Received: May 8, 1987)

Redox equilibria between RS $^{\bullet}$ and -S-S $^{-}$ radicals, and between these types of radical and phenoxyl and chlorpromazine (CIPz $^{2+}$) radicals, have been investigated in aqueous solutions at pHs over the range 6-10 to obtain a self-consistent set of redox potentials for the reactions PhO $^{\bullet}$ + H $^+$ + e $^{-}$ = PhOH (4), RSSR $^{-}$ + 2H $^+$ + e $^{-}$ = 2RSH (11), and RS $^{\bullet}$ + H $^+$ + e $^{-}$ = RSH (18), in sulfur systems with alkyl R groups. Absolute standard potentials were calculated on the basis of E° = 0.83 V for the chlorpromazine couple. The results for E°_4 (= 1.35 \pm 0.02 V) and E°_{18} (= 1.33 \pm 0.02 V) were in agreement with values calculated from thermodynamic data within the known uncertainties. E°_{18} was found to exhibit a falloff when electron-rich groups, such as the two methyls of penicillamine or the CO $_2^{-}$ of β -mercaptoacetic acid, were present on the carbon adjacent to the S atom. However, the effect was relatively small (~ 10 -14 mV). E°_{11} was 1.72 \pm 0.02 V for β -mercaptoethanol. The corresponding potentials for the cyclic anions of dithiothreitol, dithioerythritol, and lipoamide were the same within experimental error, but the uncertainties were larger (± 0.04 V). For the reaction e $^{-}$ + -S-S- = -S-S $^{-}$ (22), the magnitude of E°_{22} was calculated to be -1.60 V, showing that only strongly reducing species could donate electrons to disulfide. Rate constants for several of the forward and backward reactions in the equilibria were also determined.

Introduction

Sulfhydryl radicals (RS $^{\bullet}$ species) are of interest in the redox chemistry of inorganic^{1,2} and bioinorganic^{3,4} sulfur-containing systems. Also, these radicals and the disulfide anions (RSSR $^{-}$) formed on their complexation by thiolate anion are involved in protection mechanisms for biological systems subjected to ionizing radiation or other forms of free radical damage.^{5,6} In all of these systems a knowledge of the redox potentials is of great value in assessing various mechanisms of reaction and estimating reaction rates.

Recently we reported thermodynamic calculations⁷ that gave values of E° for the couples RS $^{\bullet}$ /RS $^{-}$, RSSR $^{-}$ /2RS $^{-}$, and

RSSR/RSSR $^{-}$. With these as a guide, experiments were designed to equilibrate different radical systems with each other and with couples of known reduction potential, so that more exact experimental E° values could be obtained. This paper reports a study of the equilibria between several sulfur-containing radicals, chlorpromazine, and phenol. In addition, the effects of structure of the aliphatic R groups of various thiyl or sulfhydryl radicals have been examined. The technique employed was pulse radiolysis. The reactions producing the radicals are well documented,^{8,9} and the procedures were the same as those described in ref 10 and 11.

As in many studies of this kind all solvated electrons (e $^{-}_{aq}$) were converted to $^{\bullet}$ OH radicals by reaction with N $_2$ O.^{8,9} Concentrations of solutes were adjusted so that those radicals reacted with either a sulfhydryl molecule (RSH) or phenol (PhOH) on a 10 $^{-7}$ -s time scale. The thiyl or phenoxyl (PhO $^{\bullet}$) radicals, which are respectively produced in the two cases, then initiated the exchange

(1) Dilworth, J. R. *Studies in Inorganic Chemistry*; Muller, A.; Krebs, B., Eds.; Elsevier: Amsterdam, 1984; Vol. 5, p 141.

(2) Lappin, A. G.; McAuley, A. *J. Chem. Soc., Dalton Trans.* 1975, 1560.

(3) Hemmerich, P.; Lauterwein, H. *Inorganic Biochemistry*; Eichorn, G. L., Ed.; Elsevier: Amsterdam, 1973; Vol. 2, Chapter 32.

(4) Fee, J. A. *Struct. Bonding (Berlin)* 1975, 23, 1. Kuehn, C. G.; Isied, S. S. *Prog. Inorg. Chem.* 1980, 27, 153.

(5) (a) Forni, L. G.; Wilson, R. L. *Biochem. J.* 1986, 240, 897. (b) Wilson, R. L.; Dunster, C. A.; Forni, L. G.; Gee, C. A.; Kittridge, K. *J. Philos. Trans. R. Soc. London, B* 1985, 311, 545.

(6) Armstrong, D. A.; Buchanan, J. D. *Photochem. Photobiol.* 1978, 28, 743.

(7) Surdhar, P. S.; Armstrong, D. A. *J. Phys. Chem.* 1986, 90, 5915.

(8) Draganić, I. G.; Draganić, Z. D. *The Radiation Chemistry of Water*; Academic: New York, 1971.

(9) Adams, G. E.; Wardman, P. *Free Radicals in Biology*; Pryor, W. A., Ed.; Academic: New York, 1977; Vol. 3, Chapter 2.

(10) Surdhar, P. S.; Ahmad, R.; Armstrong, D. A. *Can. J. Chem.* 1984, 62, 580.

(11) Surdhar, P. S.; Armstrong, D. A.; Massey, V. *Can. J. Chem.* 1986, 64, 67.